High Power Laser Science and Engineering, (2024), Vol. 12, e93, 8 pages.
doi:10.1017/hpl.2024.77

HIGH POWER LASER SCIENCE AND ENGINEERING

RESEARCH ARTICLE

Tailoring coherent beam combined laser pulse trains for high peak and average power applications

Claude-Alban Ranély-Vergé-Dépré[1,2], Corentin Lechevalier[1], Jordan Andrieu[1], Ihsan Fsaifes[1], Igor Jovanovic[3], and Jean-Christophe Chanteloup[1]

[1]*LULI, CNRS, École Polytechnique, CEA, Sorbonne Université, Institut Polytechnique de Paris, Palaiseau, France*

[2]*Thales LAS France SAS, Elancourt, France*

[3]*Gérard Mourou Center for Ultrafast Optical Science, University of Michigan, Ann Arbor, MI, USA*

(Received 4 July 2024; revised 15 October 2024; accepted 29 October 2024)

Abstract

Laser systems based on coherent beam combination (CBC) that rely on tiled pupil architecture intrinsically carry digital capabilities independently applicable to all three essential characteristics of a laser pulse: amplitude, phase and polarization. Those capabilities allow the far-field energy distribution to be flexibly tailored in real time. Operation in the femtosecond regime at high repetition rates gives access to a wide range of applications requiring both high peak and average powers. We address the task of independent peak versus average power adjustment needed for applications seeking to decouple nonlinear phenomena associated with GW peak power from the thermal load inherent to kW average power operation. The technical solutions proposed are presented in the framework of the Ecole Polytechnique XCAN CBC laser platform (61 independent channels) with an emphasis on thermal management measures implemented to ensure its nominal operation.

Keywords: coherent beam combination; digital laser; laser on demand; laser power management; optical chopper

1. Introduction

Optimizing laser systems to produce high average or high peak power for serving high-power laser users and applications is a Cornelian choice that has been largely superseded by recent technical progress made in laser amplifier design. Saraceno *et al.* (Figure 1 in Ref. [1]) highlight that the average power of the approximately kW limit for pulsed lasers is now surpassed by lasers based on three major amplifier geometries: slabs, disks and fibers. Among these, fiber optics offer the greatest potential in terms of scalability. Their mechanical flexibility and large heat exchange surface make them indeed ideal candidates for innovative architectures like those required for coherent beam combination (CBC), where many amplifiers produce parallel beams in a limited volume[2]. In the kW average power regime, the wall plug efficiency η_{wp} becomes a crucial parameter. Thanks to efficient laser diodes ($\eta_{wp} > 50\%–70\%$), pump losses have been dramatically reduced in recently developed fiber amplifiers. Selecting an optimal doping ion (Yb^{3+}, Er^{3+}, Tm^{3+}, …) to be hosted in the silica matrix of an optical fiber also contributes to improved efficiency. With a quantum efficiency of $\eta_q = 94\%$, it is no surprise that Yb-doped optical fiber is the building block of choice for fiber lasers and especially CBC laser systems.

The rise in average power is intrinsically linked to and limited by the overall efficiency of laser systems and the associated thermal management. We provide an overview of technical solutions implemented on the Ecole Polytechnique XCAN digital CBC laser to achieve efficient thermal management and address users' need to independently adjust the peak and average power. Such tailoring of laser output is a crucial part of the laser's evolution toward a versatile user platform. The digital aspect conferred by individual control of amplitude and phase[3] and recent developments in polarization control[4] is one essential aspect of this. The XCAN amplification section resides within the chirped-pulse amplification (CPA) architecture such that the seed pulse is split after stretching, and the split amplified channels are recombined into a single beam before compression. Thanks

Correspondence to: J.-C. Chanteloup, LULI, CNRS, École Polytechnique, CEA, Sorbonne Université, Institut Polytechnique de Paris, 91120 Palaiseau, France. Email: jean-christophe.chanteloup@polytechnique.fr

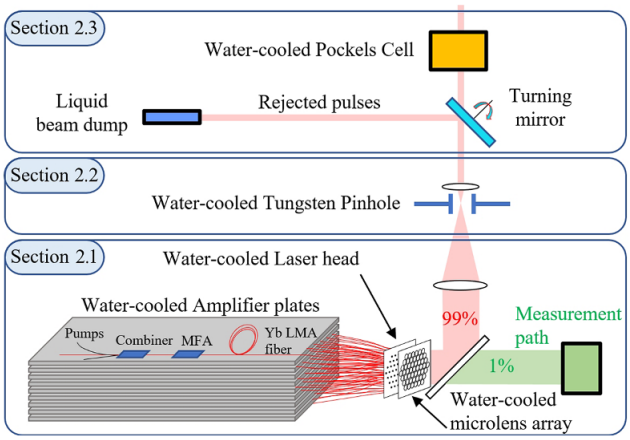

Figure 1. Schematic diagram of the laser system amplifier and free space propagation. Subjects of Sections 2.1–2.3 of this paper are identified from bottom to top. The 61 amplifying fibers are represented in red coming out from a set of nine cooled plates between which they are distributed before converging to form a bundle within the laser head (Section 2.1). While a small fraction (in green) of the light is diverted toward a measurement path dedicated at the servo loop control for CBC, the main beam (in red) undergoes a spatial selection (Section 2.2) followed by a temporal selection within the pulse train (Section 2.3).

to a cascaded chirped fiber Bragg grating (CFBG) stretcher and post-compression, XCAN offers a wide range of pulse durations. The stretcher relies on 12 CFBG fibers allowing 416 ps of stretching each, resulting in 13 distinct pulse durations between 0.4 and 5 ns. A standard reflective grating pair compressor reduces the pulse duration to approximately 300 fs, while a subsequent nonlinear post-compression stage[5] leads to 60 fs output. Independent control of average and peak power also contributes to system versatility, offering full spatial, temporal, vectorial, energetic and power control to users.

While Section 2.1 illustrates water-cooled solutions implemented at the amplifier and laser head level and presents CBC far fields recorded with such thermal management approaches, Section 2.2 summarizes water-cooled pinhole material studies. Finally, Section 2.3 explains how independent control of average and peak powers can be achieved through the combined use of a fast spinning mirror and a water-cooled Pockels cell. The schematic diagram in Figure 1 helps in visualizing where and how the proposed technical solutions are implemented within the laser system.

2. Experimental implementations and developments

2.1. *Amplifier and laser head*

The 61 amplifying stages key elements (combiners, mode field adaptors (MFAs) and large mode area (LMA) fibers[2]) rest on a set of nine aluminum plates actively cooled through water circulating into a built-in copper duct (top of Figures 2(b) and 2(c)). Without water cooling, temperatures as high as 75°C were recorded, while the temperature is limited to about 25°C maximum with flowing coolant. More aggressive thermal management had to be implemented at the laser head that contains 61 fiber amplifier outputs (Figure 2) with up to 25 W of pulsed extracted light at 1030 nm and up to 1 W of unabsorbed continuous wave pump light at 976 nm per channel. For all channels, this sums up to 1.5 kW total average power over a 6.5 cm^2 transverse section of the laser head where the fiber-to-fiber pitch is 3.2 mm. Ensuring a highly stable individual beam position and pointing accuracy (μm and mrad scales, respectively) at this stage is mandatory for an efficient CBC[6].

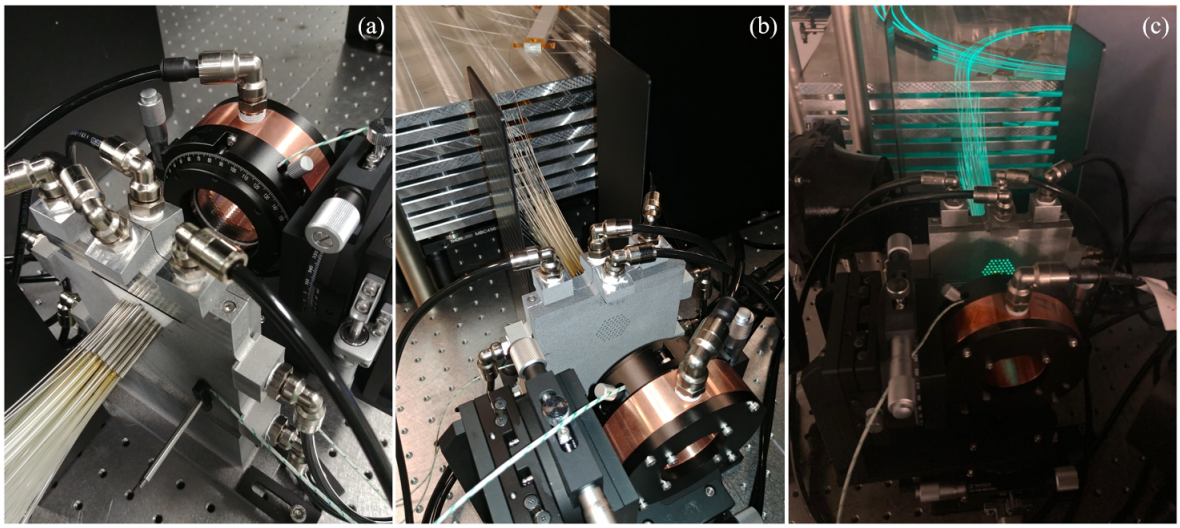

Figure 2. Three-dimensional printed water-cooled laser head hosting sleeves (white zirconium cylinder) in a V-shaped holder. Ferule-equipped fiber ends are inserted into the sleeves for accurate alignment. Downstream of the laser head, the water-cooled copper microlens array mount can be seen, while upstream the laser head, the nine water-cooled fiber amplifier supporting plates can be observed. (a) Back side and (b) front side views; (c) front side with Yb-doped fiber fluorescence.

https://doi.org/10.1017/hpl.2024.77 Published online by Cambridge University Press

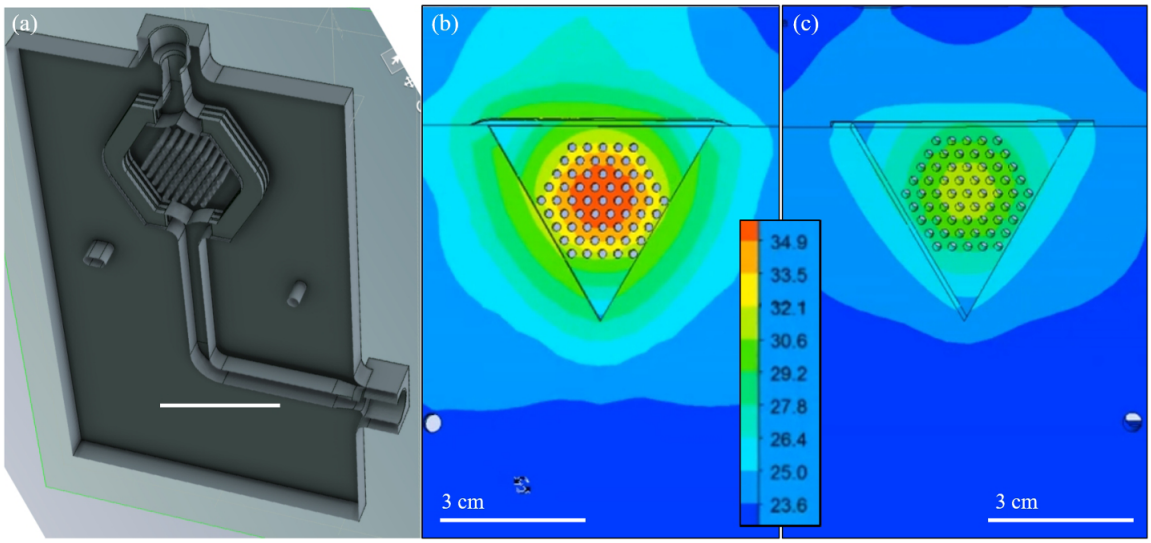

Figure 3. CAD view of the 61-hole plate collecting the unabsorbed 976 nm CW pump light refracted through the fiber end-cap (a). The cooling channel is split into two subchannels to maximize surface exchange and optimize heat removal. Thermal modeling shows a 14°C thermal gradient for single-channel cooling ducts (b), while it reveals a 10°C thermal gradient for split channel cooling ducts (c). A heat source of approximately 1 W per hole was considered in the model.

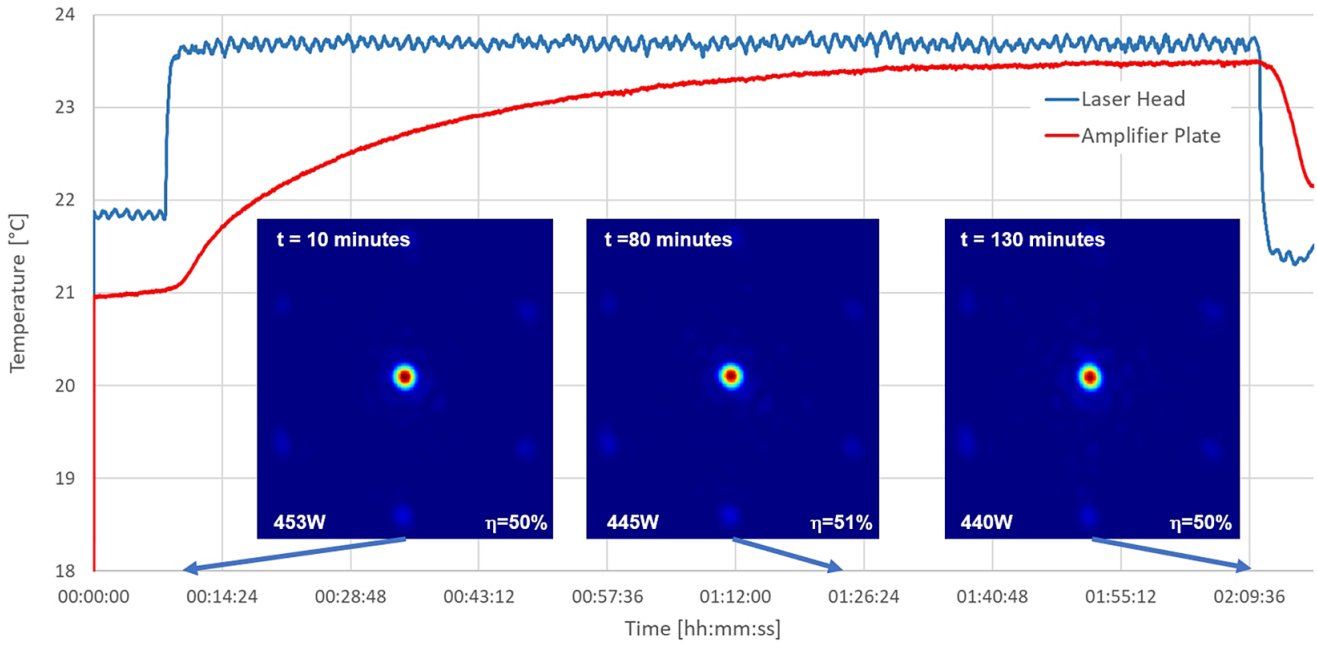

Figure 4. Temperature evolution over a 2-hour period recorded through PT100 thermal probes fixed at an amplifier plate (red) and the laser head (blue). Far fields recorded in the pinhole plane are displayed a $t = 10$, 80 and 130 minutes. The pump was set at 5 A at $t = 8$ minutes. The repetition rate is 55 MHz and a 50% stable efficiency is recorded, leading to approximately 220 W average power beam after the pinhole.

Most of the optical mounts along the subsequent beam path, including those that contain the collimated microlens array, 2-inch lens and mirrors, are water cooled as well.

Such a holistic and proactive approach to thermal management is needed since the final combined single beam stability is crucial for subsequent laser stages to perform adequately: stability affects central lobe pinhole selection centering, chopper/Pockels cell (see Section 2.3) power management stage tailoring, alignment of compressor and post-compression cells[7], frequency conversion and final focusing. Together, these measures limit the beam deviation to about 10% of its diameter.

The laser head is an optomechanical assembly that poses most severe demands on the heat management. It consists of three-dimensional (3D) printed aluminum elements carefully adjusted with respect to each other. Thanks to metal additive manufacturing it is possible to internally structure the cooling ducts to maximize the heat exchange coefficient for

https://doi.org/10.1017/hpl.2024.77 Published online by Cambridge University Press

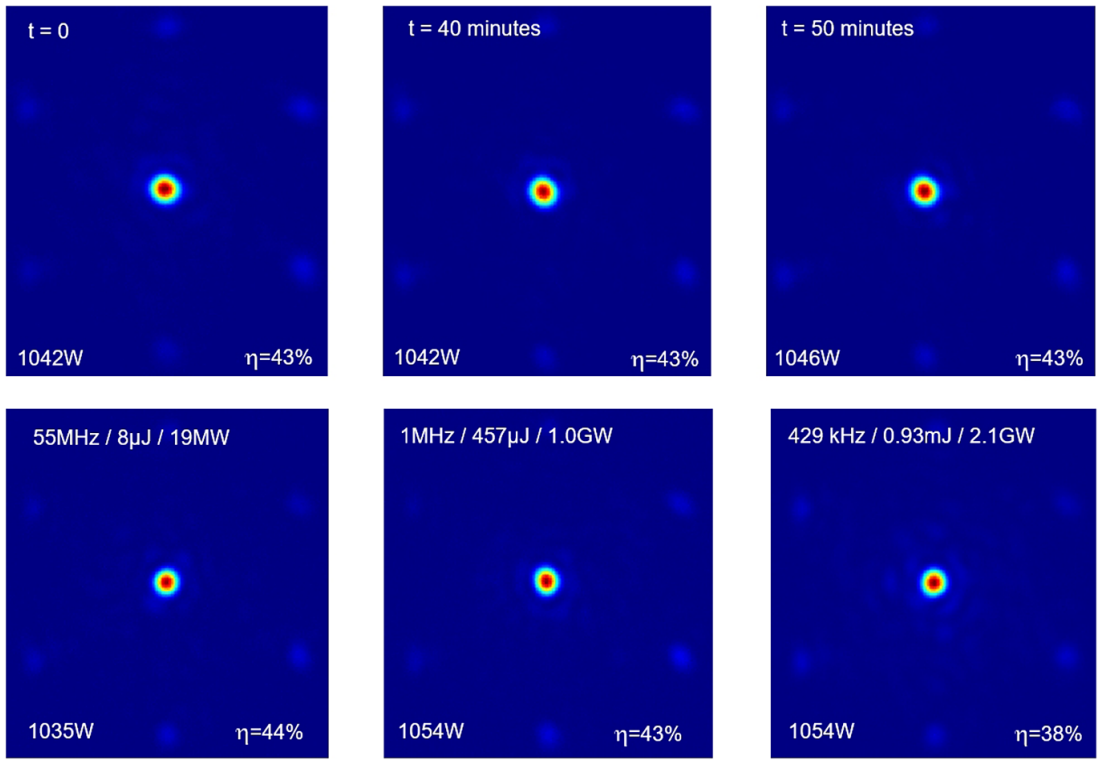

Figure 5. Far fields recorded in the pinhole plane in kW average power regime (bottom left values). The top three images are obtained at a 55 MHz repetition rate over a 50-minute period. The bottom three images are obtained at 55 MHz, 1 MHz and 429 kHz repetition rates, respectively. Energy in the main lobe is given as well as peak power after compression at 350 fs.

optimum thermal load removal. Figure 3 shows an internal computer-aided design (CAD) view of the split duct that reduces the thermal gradient by approximately 30%.

Respective cooling efficiencies at an amplifier plate and the laser head level can be compared in Figure 4 where far fields recorded in the pinhole plane are displayed. At $t = 8$ minutes the CW diode pump operating current was instantaneously increased from 2 to 5 A, bringing the total optical power from 67 W to about 450 W. While the laser head is thermally stabilized within 1 minute, it takes about 1 hour for the amplifier plate. The temperature amplitude variation is really weak, especially when compared with the previous 75°C reached without water cooling of the plates.

Figure 5 (top three images) reveals a 7% drop in efficiency when operating at the kW level (pump diode operating current set at 8.6 A) with a stable 43% value over a 1-hour period (at 55 MHz repetition rate). Amplifier plates and laser head temperatures (not displayed) stabilized respectively at 24.1°C and 24.4°C, that is, less than a degree above the temperatures recorded at half this average power (Figure 4). The bottom three images are recorded with decreasing repetition rates (55, 1 and 0.5 MHz, respectively), allowing the energy per pulse to increase up to approximately 1 mJ in the central lobe. Operation at such energy level means a rather strong nonlinear regime with an estimated B-integral level above 3 radians. It is likely to explain the extra 5% drop observed in the efficiency. After the pinhole a 400 W average power pulse train is sent toward the compressor (~80% transmission) to reach 2.1 GW peak power (350 fs pulse duration).

2.2. *Central lobe selection*

XCAN laser relies on 61 Yb-doped LMA fiber amplifiers combined in a tiled aperture architecture (also known as far-field combining). CBC is performed with the help of a single optic: a large (2 inch) aperture lens that collects all 61 3.2 mm-spaced adjacent sub pupils. At the lens focal plane, the central lobe theoretically concentrates up to 66% of the total power. The remaining power is distributed mainly into six surrounding lobes, carrying about 5% of the total power each. In practice, around 50% of the energy is contained in the central lobe, a value that can decrease to 40% when operating in the kW average power regime; in addition a non-negligible amount of power lies in a diffuse speckle between the central and the six surrounding lobes. A pinhole is placed in the focal plane to block the speckle light and deliver a clean TEM00 beam to users.

To maintain the pinhole integrity over long operation time, it is placed in a water-cooled mount. Then, one needs to make sure it is made of a material that is able to sustain high average power delivered in the nanosecond regime. Finally, one has to make sure the surrounding lobes are not focusing outside the pinhole. Several materials were tested: stainless steel (316L), tungsten-lanthanum oxide

https://doi.org/10.1017/hpl.2024.77 Published online by Cambridge University Press

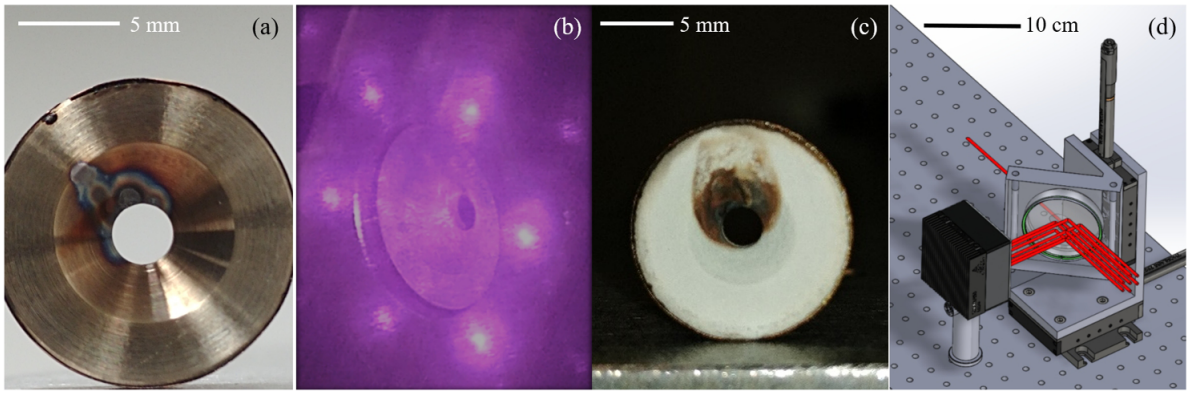

Figure 6. (a) Stainless-steel pinhole with the onset of melting at 440 W average power operation. (b) Impact of surrounding lobes on the tungsten pinhole mount. (c) ZrO_2 coated pinhole. (d) CAD view illustrating surrounding beam deviation toward a beam dump.

(WL10) and zirconium oxide (ZrO_2), with respective fusion temperatures of 1400°C, 2715°C and 3420°C. Whereas the stainless-steel pinhole started melting quickly (at 440 W average power level, see Figure 6(a)), no degradation of the tungsten pinhole (Figure 6(b)) was observed even at maximum power (880 W). The ZrO_2-coated stainless-steel pinhole sustained greater average power than the uncoated stainless-steel pinhole, with the onset of burning observed at 570 W (Figure 6(c)). At some point (average power way above the kW regime), a single WL10 pinhole is likely to face a melting issue as well and schemes based on double slits (stretching out the heated area to two successive lines instead of a single focal point) might be required[8].

Figure 6(b) illustrates that the surrounding lobes impact the pinhole mount significantly. To prevent this, a 45° holed mirror is introduced on the converging composite beam in its way to the coherent combination (Figure 6(d)). The 13 mm mirror hole diameter is located 50 cm before the pinhole. Unwanted beams are directed toward a dedicated beam dump consisting of a reservoir with circulating water. A window with appropriate antireflective coating ensures an efficient coupling into the water (absorption coefficient at 1 μm is $\alpha \sim 20\ m^{-1}$). Such a beam dump allows efficient average power management while eliminating the creation of dust particles at the laser–solid interface (as on solid beam dumps). Dumping these beams is not the only possibility; a two-step CBC[9] scheme has been envisioned, where these six beams that are already in phase are coherently added, offering a second beam to users.

2.3. Average power adjustment at constant peak power

The XCAN front end relies on an oscillator delivering nJ pulses at 55 MHz. Three acousto-optic modulators are inserted as pulse pickers to reduce the repetition rate. XCAN laser amplifiers are CW pumped at 976 nm with up to 60 W per amplifier. Consequently, a decrease in repetition rate implies a proportional increase in pulse energy. At lower repetition rates, typically a few hundred kHz, the output energy per channel reaches values that do not allow efficient operation of the laser system. Above 75 μJ, a 2.5 ns pulse amplified through the 1.6 m long silica fiber with a 30 μm diameter mode accumulates a significant nonlinear phase (≫3 rad). The XCAN servo loops can compensate phase and delay perturbations (thermal drifts, mechanical vibrations, acoustic noises, …) from channel to channel up to a 400 Hz effective bandwidth and then efficiently keep coherence between them. However, nonlinear phase variations are almost instantaneous (they occur on the fs scale) and cannot be corrected. It is therefore mandatory to operate in an energy regime that does not lead to excessive B-integral (up to 5–6 rad). Typically, the XCAN operating repetition rate is set at 333 kHz. With a 1 mJ pulse, this leads to 333 W average power, and 300 fs compressed pulses lead to 3 GW peak power.

Certain experimental configurations and applications require decoupling average from peak power adjustment. High repetition rate operation can induce thermal effects that obscure both the observation and analysis of a specific high peak power phenomenon (e.g., nonlinear effects). One can also consider experiments involving several laser beams (pump–probe) and/or relying on evolving targets (gas, liquid, droplet jets), where nominal peak power is necessary without the nominal pulse repetition rate. Also, the motivation for decoupling occurs in the area of materials processing where one may want to use a single pulse or a tailored burst of pulses to perform some material processing tasks, such as drilling a small hole or removing the surface to a set depth.

Deriving a technical solution to adjust the pulse repetition of the laser while keeping a nominal peak power appears therefore beneficial for such research and industrial needs.

A Pockels cell can select a single pulse from a MHz pulse train (in the XCAN nominal configuration pulses are separated by 3 μs), but the electro-optic crystal (e.g., potassium dideuterium phosphate (KD*P), potassium titanyl phosphate (KTP), beta barium borate (BBO), $LiNbO_3$) at the core of

https://doi.org/10.1017/hpl.2024.77 Published online by Cambridge University Press

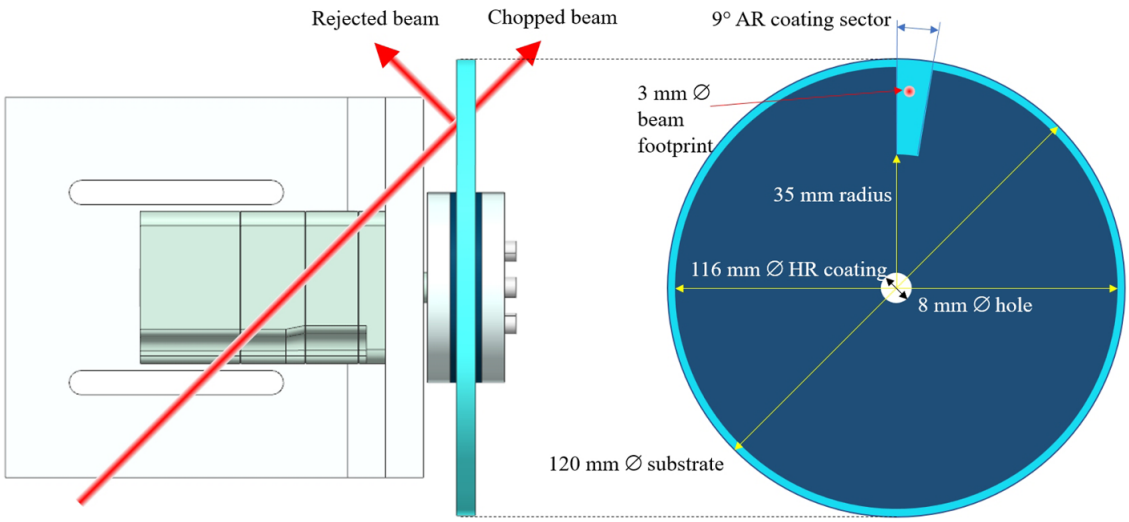

Figure 7. AR/AR coated 9° angular segment in an AR/HR 120 mm diameter disk.

such optical switch suffers from residual absorption, leading to an internal temperature rise degrading the quality of the transmitted laser polarization adjustment as well as beam quality. Properly designed BBO Pockels cells can sustain several hundred watts of average power, but large aperture (>10 mm) BBO crystals are costly and two of them must be used in series to lower the drive voltage to a realistic value. Even so, two 10 mm × 10 mm × 20 mm crystals in series still have a half-wave voltage of approximately 11.3 kV. A KD*P Pockels cell prototype was operated at kW average power[10] thanks to an efficient but rather complex cooling architecture: a continuous flow of helium is circulating through four slices of crystal, an approach not suitable for most users.

We opted therefore for a KD*P crystal-based Pockels cell from Leysop (EM510M series), which is an order of magnitude less expensive (even not considering the additional cost of a second Pockels cell driver) than a BBO cell. Transmissions of dielectrically coated BBO faces and windows are respectively 99.7% and 99.6% over a 970–1100 nm bandwidth. Knowing that a typical KD*P crystal-based Pockels cell can operate efficiently up to a few watts of average power at a 1 μm wavelength, a complementary solution is needed when dealing with several hundreds of watts. For that purpose, we have developed a homemade chopper with a 2.5% transmission ratio, which is placed upstream from the Pockels cell. Standard metallic choppers cannot be used since they are unable to sustain absorption at a level of hundreds of watts. A partially reflective rotating wheel is used instead. To minimize any vibration imprinted on the laser beam, the chopper reflects the unwanted fraction of the incoming pulse train, while the burst of pulses used for experiments is transmitted through the chopper. To avoid potential air turbulence impacting a beam passing through any angularly cut fast rotating mirror[11], we use a highly reflective/antireflective coated fused silica disk according to the design displayed in Figure 7. Naneo Precision IBS coatings GmbH optimized the coatings with $T > 99.5\%$ (antireflection) and $R > 99.5\%$ (high reflection) over a 970–1100 nm bandwidth.

The motor (Yaskawa S7) maximum rotation rate is set at 6000 r/min. At this repetition rate (100 Hz), each 10 ms, a 250 μs long burst containing 82 pulses separated by 3 μs (at the laser repetition rate of 333 kHz) is transmitted by the chopper. At 10 Hz, the 2.5 ms long bursts are separated by 100 ms and contain 825 pulses. Whatever the rotating speed, the average power is reduced to $9°/360° = 2.5\%$ of the incident power. For instance, a 165 W average power 333 kHz pulse train carries a 4 W average power when reaching the Pockels cell. Figure 8 displays the linearly polarized pulse sequences entering the Pockels cell when the laser is operated at 333 kHz and the mirror rotation is set at 31 Hz. A Thorlabs DET08CFC 5 GHz photodiode is used to record the pulse train. Leading and falling front slopes are related to the beam transverse shape (Gaussian), size (3 mm at $1/e^2$), radial position (50 mm from center) and mirror rotating rate (31 Hz). Negative and positive overshoots are related to the photodiode operation.

Figure 9 displays the Pockels cell output pulse train when applying a 111 μs, 7 kV voltage square signal onto the Pockels cell electrodes. A series of 37 pulses (still 3 μs spaced) has then been selected out of each burst, as illustrated in Figure 8 (bottom right). Figure 10 shows a single pulse selection with a 200 ns, 7 kV voltage square signal. Extracting a single pulse from each burst produces pulse trains with repetition rates between 1 and 100 Hz, where the upper limit is set by the maximum chopper rotation rate. All traces have been recorded with a Tektronix MDO34 1 GHz oscilloscope.

https://doi.org/10.1017/hpl.2024.77 Published online by Cambridge University Press

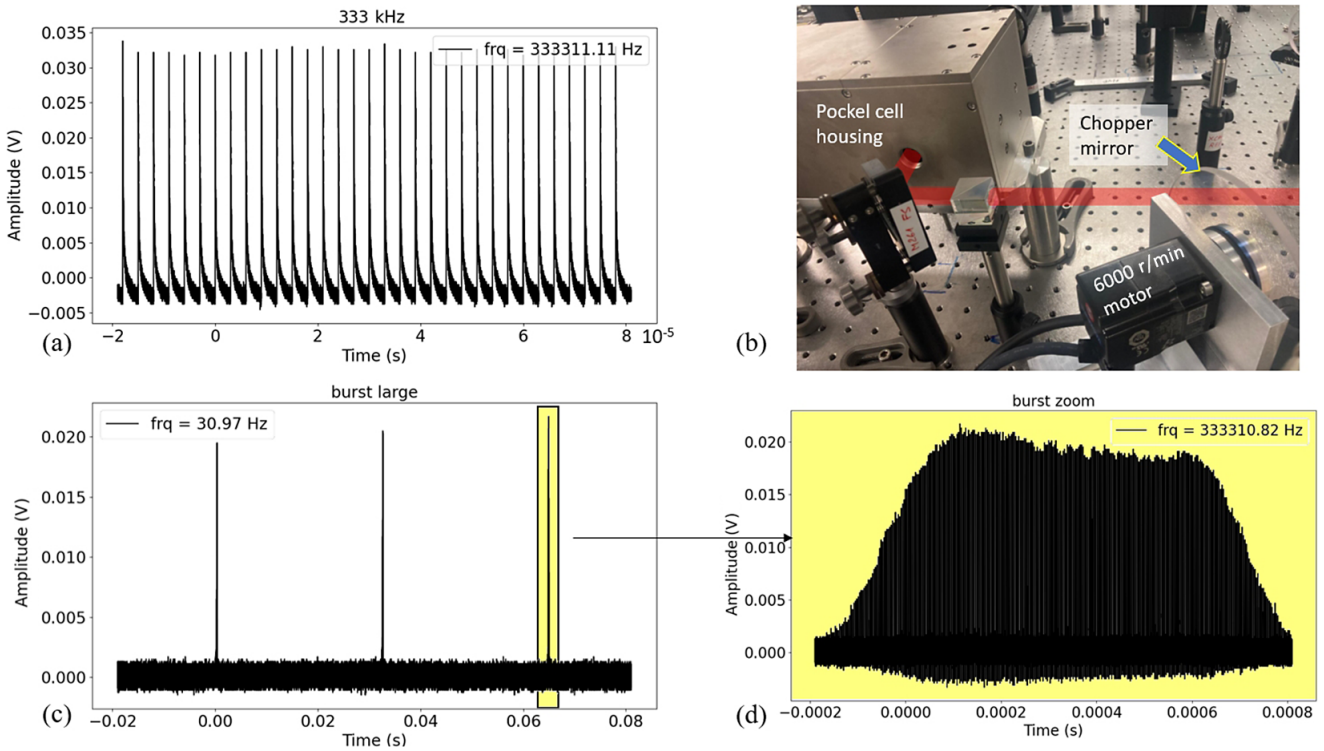

Figure 8. (a) Pulse train within the burst at 333 kHz. (b) Motor and mirror assembly (front right) and Leysop 1000:1 extinction ratio Pockels cell housing (back left). (c) 31 Hz burst train. (d) Single burst.

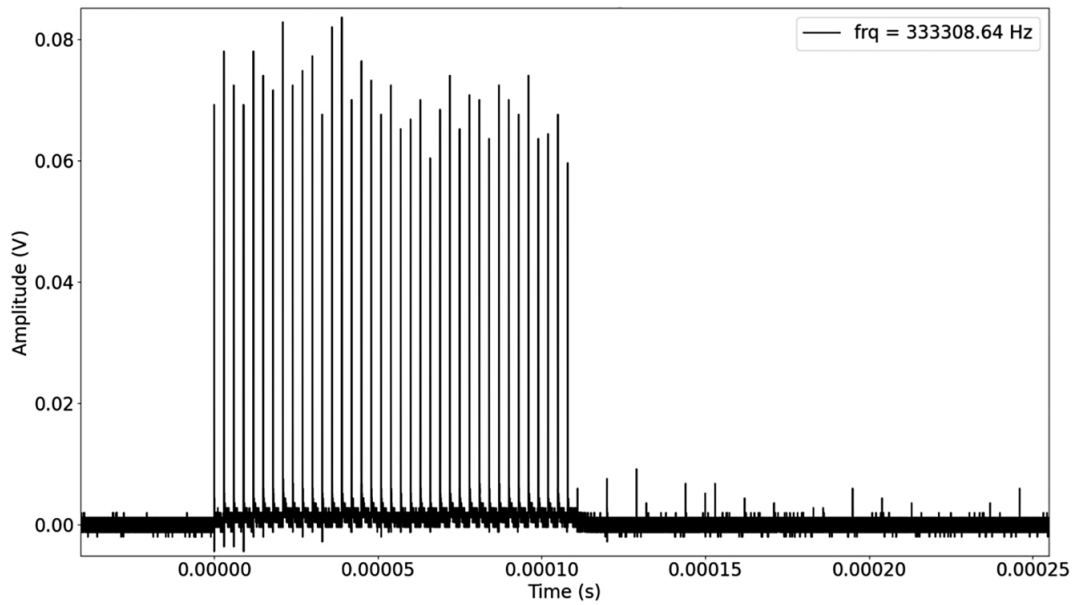

Figure 9. Pockels cell output pulse train recorded with a Thorlabs DET08CFC 5 GHz photodiode when applying a 111 μs, 7 kV voltage square signal onto the KD*P electrodes. A series of 37 pulses can be observed. The contrast exceeds 1:100, evaluation being limited by the residual noise level on the photodiode. A few erratic parasitic signals appear on the trailing edge.

3. Conclusion

Thermal management solutions specific for CBC were developed with an additive processed laser head hosting several dozens of fibers and a far-field beam selection with a tungsten pinhole coupled to a holed mirror and a water beam dump. An innovative technical solution was designed, validated and implemented on the XCAN CBC laser to independently manage the peak and average laser power, which is needed for laser–matter interaction applications. The combined use of an optical chopper and a standard Pockels cell addresses that goal while expanding the range

https://doi.org/10.1017/hpl.2024.77 Published online by Cambridge University Press

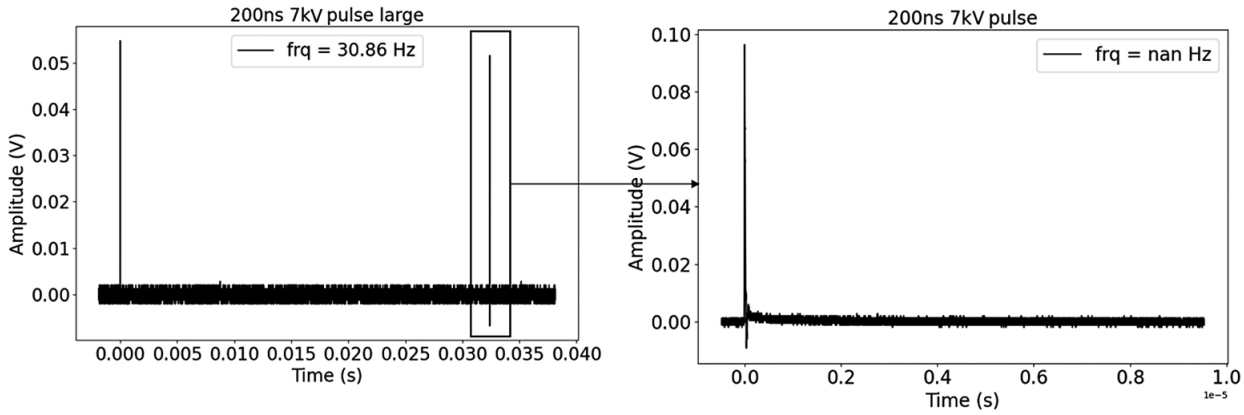

Figure 10. Single pulse extraction from the 31 Hz burst.

of repetition rates made available to users. Altogether, these developments allow a simultaneous kW/GW average/peak power operation with independent adjustability.

Acknowledgements

The authors would like to thank the Laboratoire Interdisciplinaire Carnot de Bourgogne (https://lermps.utbm.fr/) for depositing zirconium on our steel holes as well as Thales LAS for performing the laser head thermal modeling.

This work received funding from the European Innovation Council (Open grant No. 101047223-NanoXCAN and Horizon 2020 Framework Programme 654148), the Agence de l'Innovation de Défense (AID) and the Centre National des Etudes Spatiales (CNES).

This work was supported in part by the U.S. Department of Defense, Defense Threat Reduction Agency (HDTRA1-20-2-0002).

References

1. C. J. Saraceno, D. Sutter, T. Metzger, and M. A. Ahmed, J. Eur. Opt. Soc.-Rapid Publ. **15**, 15 (2019).
2. I. Fsaifes, L. Daniault, S. Bellanger, M. Veinhard, J. Bourderionnet, C. Larat, E. Lallier, E. Durand, A. Brignon, and J.-C. Chanteloup, Opt. Express **28**, 20152 (2020).
3. M. Veinhard, S. Bellanger, L. Daniault, I. Fsaifes, J. Bourderionnet, C. Larat, E. Lallier, A. Brignon, and J.-C. Chanteloup, Opt. Lett. **46**, 25 (2021).
4. C. Lechevalier, C.-A. Ranély-Vergé-Dépré, I. Fsaifes, R. Becheker, G. Boer, and J.-C. Chanteloup, IEEE Photonics J. **16**, 1502305 (2024).
5. L. Lavenu, M. Natile, F. Guichard, Y. Zaouter, X. Delen, M. Hanna, E. Mottay, and P. Georges, Opt. Lett. **43**, 2252 (2018).
6. A. Heilmann, J. Le Dortz, L. Daniault, I. Fsaifes, S. Bellanger, J. Bourderionnet, C. Larat, E. Lallier, M. Antier, E. Durand, C. Simon Boisson, A. Brignon, and J.-C. Chanteloup, Opt. Express **26**, 31542 (2018).
7. I. Fsaifes, C. Ranély-Vergé-Dépré, R. Becheker, K. Fritsch, O. Pronin, and J. Chanteloup, in *Laser Congress 2023 (ASSL, LAC)*, Technical Digest Series (Optica Publishing Group, 2023), paper ATh3A.1.
8. H. Xiong, X. Yuan, X. Zhang, and K. Zou, Opt. Express **22**, 22211 (2014).
9. I. Fsaifes, C.-A. Ranély-Vergé-Dépré, M. Veinhard, S. Bellanger, and J.-C. Chanteloup, Opt. Express **31**, 8217 (2023).
10. L. F. Weaver, C. S. Petty, and D. Eimerl, J. Appl. Phys. **68**, 2589 (1990)
11. X. Li, T. Scott, C. Cromer, and J. Hadler, J. Res. Natl. Inst. Stand. Technol. **113**, 305 (2008).

https://doi.org/10.1017/hpl.2024.77 Published online by Cambridge University Press